Chemical Science

ROYAL SOCIETY OF CHEMISTRY

EDGE ARTICLE

View Article Online
View Journal | View Issue



Cite this: *Chem. Sci.*, 2024, **15**, 14521

All publication charges for this article have been paid for by the Royal Society of Chemistry

Received 20th May 2024
Accepted 11th August 2024

DOI: 10.1039/d4sc03284e

rsc.li/chemical-science

# Surface topology of MXene flakes induces the selection of the sintering mechanism for supported Pt nanoparticles†

Jiawei Huang,[a] Yucheng Zhang,[a] Jiaqi Chen,[a] Zhouyang Zhang,[b] Chunfang Zhang,*[c] Changshui Huang*[d] and Linfeng Fei*[a]

Sintering of metal nanocatalysts leading to particle growth and subsequent performance deactivation is a primary issue that hinders their practical applications. While metal–support interaction (MSI) is considered as the critical factor which influences the sintering behavior, the underlying microscopic mechanism and kinetics remain incompletely understood. Here, by using *in situ* scanning transmission electron microscopy (STEM) and theoretical analysis, we reveal the selection rule of the sintering mechanism for Pt nanoparticles on a two-dimensional (2D) MXene ($Ti_3C_2T_x$) support, which relies on the surface topology of MXene flakes. It is demonstrated that the sintering of Pt nanoparticles proceeds *via* Ostwald ripening (OR) in the surface defect (such as steps and pore edges) regions of MXene flakes due to strong MSI on the Pt/MXene interface; conversely, weak MSI between Pt nanoparticles and the planar surface of MXene leads to prevalent particle migration and coalescence (PMC) for sintering. Furthermore, our quantitative analysis shows a significant divergence in sintering rates for PMC and OR processes. These microscopic observations suggest a clear "sintering mechanism–MSI" relationship for Pt/MXene nanocatalysts and may shed light on the design of novel nanocatalysts.

## Introduction

Modern heterogeneous catalysts are generally noble metal (Pt, Au, Pd, *etc.*) nanoparticles (NPs), or even single atoms, decorated on high-surface-area supporting materials (oxides, nitrides, carbon materials, *etc.*), which have found their wide applications in chemical production, energy transition, pharmaceuticals, and waste treatment.[1–9] Ideally, these catalytic NPs are supposed to maintain their size and dispersity under reactive (*i.e.*, thermal, chemical, *etc.*) conditions; however, sintering of metal NPs (small NPs agglomerate into large ones) always occurs on supports in practical catalytic scenarios, which reduces the nanocatalysts' active sites together with their catalytic performance.[10–14] To alleviate this sintering issue of nanocatalysts, it is thus rather essential to microscopically extract the mechanisms and kinetics underlying it; after decades of investigation, it is widely accepted that sintering of metal NPs proceeds *via* either diffusion of metal atoms and/or molecules (Ostwald ripening, OR) or particle migration and coalescence (PMC) on supports.[15–19] For example, Helveg *et al.* have provided *in situ* evidence for the OR of Pt NPs supported on $Al_2O_3$;[18] Asoro *et al.* have reported the process of coalescence and sintering for Pt NPs supported on high-surface-area carbon materials by using *in situ* aberration-corrected scanning transmission electron microscopy (STEM).[19]

Furthermore, it is worth noting that supports are not totally inert and their interaction with metal NPs (*i.e.*, metal–support interaction, MSI) plays a significant role in the sintering process.[20–23] Scientists have long realized that MSI engineering can tune the stability of supported catalysts, despite the underlying mechanism remaining mostly unknown. Lin *et al.* have engineered the MSI between Ni and the ceria support, which presented an appreciably higher (2–3 fold) catalytic activity in $CO_2$ methanation with high selectivity and stability;[24] Xin *et al.* have shown the excellent catalytic activity and long-term stability of the Ru–$MoO_3$ catalyst in selective $CO_2$ hydrogenation to CO through constructing strong MSI.[25] Recently, the kinetic simulations by Hu and Li have finally bridged the aforementioned OR/PMC sintering dynamics to this fundamental effect of MSI;[26] the authors suggest that a strong/weak MSI is respectively correlated with the OR/PMC behavior of nanocatalysts, which should be of remarkable guidance for the design of ultrastable nanocatalysts. Subsequently, the judicious choice of supporting materials is adopted as an effective handle

[a]School of Physics and Materials Science, Nanchang University, Nanchang 330031, China. E-mail: feilinfeng@gmail.com

[b]School of Materials and New Energy, Ningxia University, Yinchuan 750021, China

[c]College of Chemistry and Materials Science, Hebei University, Baoding 071002, China. E-mail: zhangcf@hbu.edu.cn

[d]Beijing National Laboratory for Molecular Sciences, Organic Solids Laboratory, Institute of Chemistry, Chinese Academy of Sciences, Beijing 100190, China. E-mail: huangcs@iccas.ac.cn

† Electronic supplementary information (ESI) available. See DOI: https://doi.org/10.1039/d4sc03284e

to tune the MSI for anti-sintering catalysts (which is now popularized as "chemical confinement").[27–32] However, the search for a suitable support for each kind of metal NPs toward a wide range of chemical reactions is, indeed, technically complex and time-consuming. In this context, another interesting question arises: is there any other approach to control MSI rather than make attempts of different supports?

Pioneering studies have suggested that surface defects and functional groups on supports are beneficial for stabilizing the catalytic NPs against sintering. As a supporting material, defect-rich carbon was found beneficial in promoting the dispersion of Ni NPs, reducing the Ni particle size, and affecting the surface charge state of Ni to form electron-deficient Ni, leading to outstanding catalytic activity from MOF-derived Ni@C catalysts.[33] Electronegative terminations on the $Ti_3C_2T_x$ MXene surface were also found to induce strong MSI with the Pd catalyst, which consequently improved the chemical stability of Pd and favorably influenced the surface electronic structure.[34] However, fundamental knowledge concerning the relationship between these surface defects and anti-sintering mechanisms is elusive for the community until now.

Recently, *in situ* (scanning) transmission electron microscopy, (S)TEM, due to its ultra-high spatiotemporal resolution and its ability to simulate the working environments, has been proven to be a versatile tool for observing nanoscale dynamics on catalysts and other nanomaterials.[35–39] Herein, by designing *in situ* STEM experiments, we reveal the selective sintering mechanism of Pt particles induced by the surface topology of MXene flakes (as the supporting material). Of note, two-dimensional MXene materials, with their unique electronic structure, excellent electrical conductivity, abundant surface terminations and structural flexibility, are emerged as a new family of supporting materials for catalytic NPs in recent studies.[40–44] And more importantly, compared to normal two-dimensional supports with a smooth surface (such as graphene), the surface of MXene is generally enriched with steps and other defects during the preparation and exfoliation,[45–48] which acts as an excellent platform as a supporting material in this study. Consequently, the sintering behaviors of Pt NPs on the MXene surface have been directly observed and quantitatively analyzed by *in situ* STEM, in which we identify that surface steps (or pore edges) and planar regions of MXene flakes are responsible for different sintering mechanisms of supported Pt NPs. Specifically, surface steps on MXene have strong MSI with Pt NPs and then lead to the OR process of NPs, whereas Pt NPs supported on planar MXene experience a typical PMC process due to their relatively weak MSI. Furthermore, our experimental results also suggest the distinct kinetics for these two processes. Our findings regarding such complex sintering dynamics on a single support provide a step forward in understanding the sintering mechanisms and kinetics of supported metal NPs and may shed light on the design of novel ultrastable MXene-based catalysts.

## Results and discussion

### Experimental design

To trace the atomic-scale sintering dynamics of Pt NPs on MXene flakes in a heating environment, it is essential to guarantee the clean interface across Pt/MXene. Therefore, the experimental protocol was designed as shown in Fig. 1a. Briefly, MXene flakes were first dispersed on a heating E-chip specimen support, which was then treated by $Ar^+/O^{2-}$ bombardment (Fig. S1† compares the STEM images of MXene flakes before and after the plasma treatment, showing no considerable change throughout the process)[49] before the dispersion of the $(NH_3)_4Pt(NO_3)_2$ precursor (see Methods for details); the precursor would later be decomposed into Pt NPs under mild conditions[50] and hence *in situ* produce Pt/MXene interfaces. Prior to the *in situ* experiment, we have systematically examined MXene flakes and Pt/MXene interfaces with aberration-corrected STEM. The morphology of a random MXene flake is shown in Fig. 1b (TEM images of more MXene flakes are also provided in Fig. S2†), which is clearly seen to be enriched with surface defects and zigzag edges as reported elsewhere.[51,52] Fig. 1c shows the HAADF (*i.e.*, high-angle annular dark-field) STEM image of a representative MXene flake with 0.15 nm interplanar distances, also suggesting the existence of surface atomic steps (highlighted by green lines) and pores (marked by yellow and red boxes) on it. High-magnification views of the pore/edge structures of MXene are further shown in Fig. 1d. The selected-area electron diffraction (SAED) pattern of an isolated MXene flake in Fig. 1e corresponds to its [001] zone axis, revealing its monocrystalline nature.

Subsequently, an aberration-corrected STEM image for the Pt/MXene interface was captured (Fig. 1f), displaying a uniform dispersion of Pt NPs (the white particulates in the image) on the MXene surface (the Pt formation from $(NH_3)_4Pt(NO_3)_2$ is attributed to the irradiation of the high-energy electron beam[53]). The bottom-right inset in Fig. 1f shows a detailed view of a typical Pt particle (approximately 1 nm in size) supported on MXene, close to those structures of Pt catalysts in previous reports.[54,55] Notably, the steps/edges on MXene flakes are practically more complex than one-dimensional atomic columns, and therefore the Pt NPs can be dispersed over the defective regions. It should be further noted that upon loading of high-density Pt NPs on their surface, the steps/pores can still be identified during observation (as shown in Fig. S3†); this is of key importance for the following *in situ* experiments.

The elemental maps for Ti and Pt together with the HAADF STEM image for the Pt/MXene interface are provided in Fig. 1g, indicating the dense and synchronous distribution of Pt NPs on MXene flakes. Moreover, the electron energy loss spectra (EELS) for the Pt/MXene interface in selected energy regions are shown in Fig. 1h (at room temperature and after heating to 500 °C). The weakening of the O–K edge after heating to 500 °C reveals the removal of $T_x$ groups from $Ti_3C_2T_x$ structures;[56] the emerged Pt–$M_5$ edge at ~2200 eV in the right panel of Fig. 1h is a sign for the formation of larger Pt NPs after heating to 500 °C (at room temperature, there are almost no peaks can be observed due to the small Pt particle size). Based on the above characterization, the Pt/MXene structure is suitable for *in situ* observation of sintering behaviors of Pt NPs on the MXene support (the schematic illustration for sintering of Pt NPs is shown in Fig. 1i).

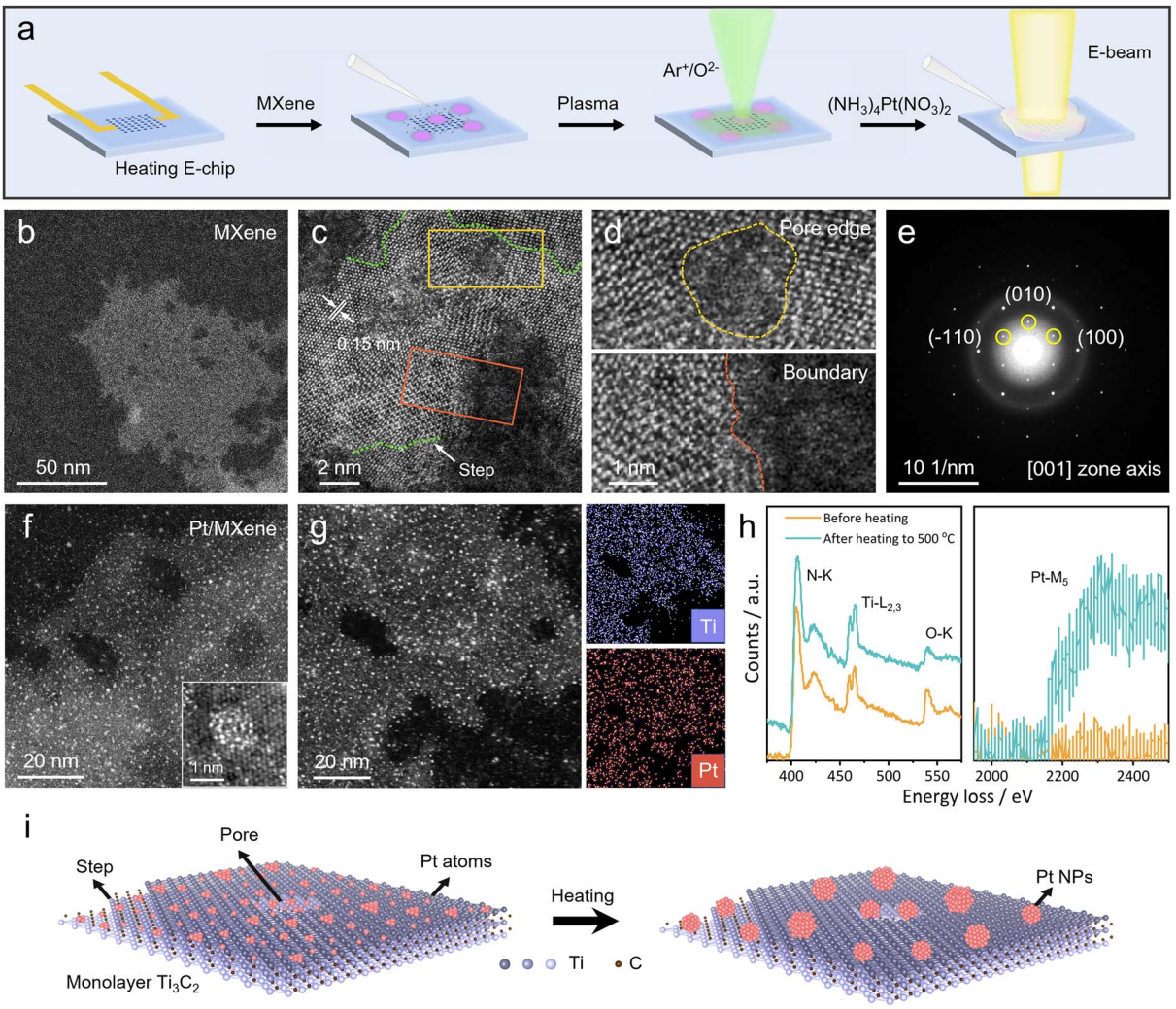


Fig. 1 Design and characterization of the Pt/MXene interface. (a) Schematic design of the *in situ* STEM experiment. (b) Typical low-magnification HADDF STEM image of a random MXene flake. (c) Magnified HAADF STEM image of a MXene flake, showing the existence of steps (marked by green lines) and pore edges (marked by yellow and red boxes) at the surface. Top and bottom panels in (d) show high-magnification views of the pore edge and boundary in (c), respectively. (e) SAED pattern of a MXene flake, showing its single-crystalline nature. (f) HAADF STEM image for Pt NPs supported on MXene flakes. The bottom-right inset in (f) shows a detailed view of a Pt NP on the MXene surface. (g) EDS elemental maps for Ti and Pt of an isolated Pt/MXene flake. (h) EELS spectra taken from a Pt/MXene flake before and after heating to 500 °C for the N–K, O–K, Ti–$L_{2,3}$ and Pt–$M_5$ edges. (i) Schematic illustration for the formation of Pt NPs on MXene flakes *via* heating.

### Sintering dynamics of Pt NPs on MXene flakes

In order to observe the sintering dynamics of Pt NPs on the MXene support, we heated the Pt/MXene sample from room temperature to 800 °C inside a TEM and *in situ* monitored its temperature-dependent structural behaviors. As shown in Fig. 2a–h, the temperature-dependent *in situ* STEM images suggest that the precipitation and growth of Pt NPs on MXene flakes occurred with rising temperatures. It is noted that Pt NPs emerged at both the planar surface and surface step sites of MXene flakes throughout the experiment. And after heating to 800 °C, the TEM image of Pt/MXene shows a uniform distribution of Pt NPs (see Fig. S4a†) with good crystallinity (see Fig. S4b and c† for the lattice-resolved HRTEM images and their corresponding fast Fourier transform (FFT) patterns).[57]

To quantitatively understand the sintering behaviors of Pt NPs on the MXene support, we analyzed the visible number and average size of Pt NPs as a function of annealing temperature. As shown in Fig. 2i, the particle number–temperature profile shows the change of the number of Pt NPs on the MXene flake. One can clearly see that the number of Pt NPs increased before 400 °C , and then dropped in the region of 400–800 °C. In combination with the synchronized size–temperature profile of Pt NPs (Fig. 2j), it is apparent that the sintering process of Pt NPs on the MXene surface can be divided into two stages (as schematically shown in Fig. 2k). The first stage of number/size increasing before 400 °C (Stage I) is simply the precipitation of Pt NPs, and the average particle size reached about 1.1 nm at 400 °C. Subsequently, the average size of Pt NPs further increased to about 1.7 nm while the total number decreased to

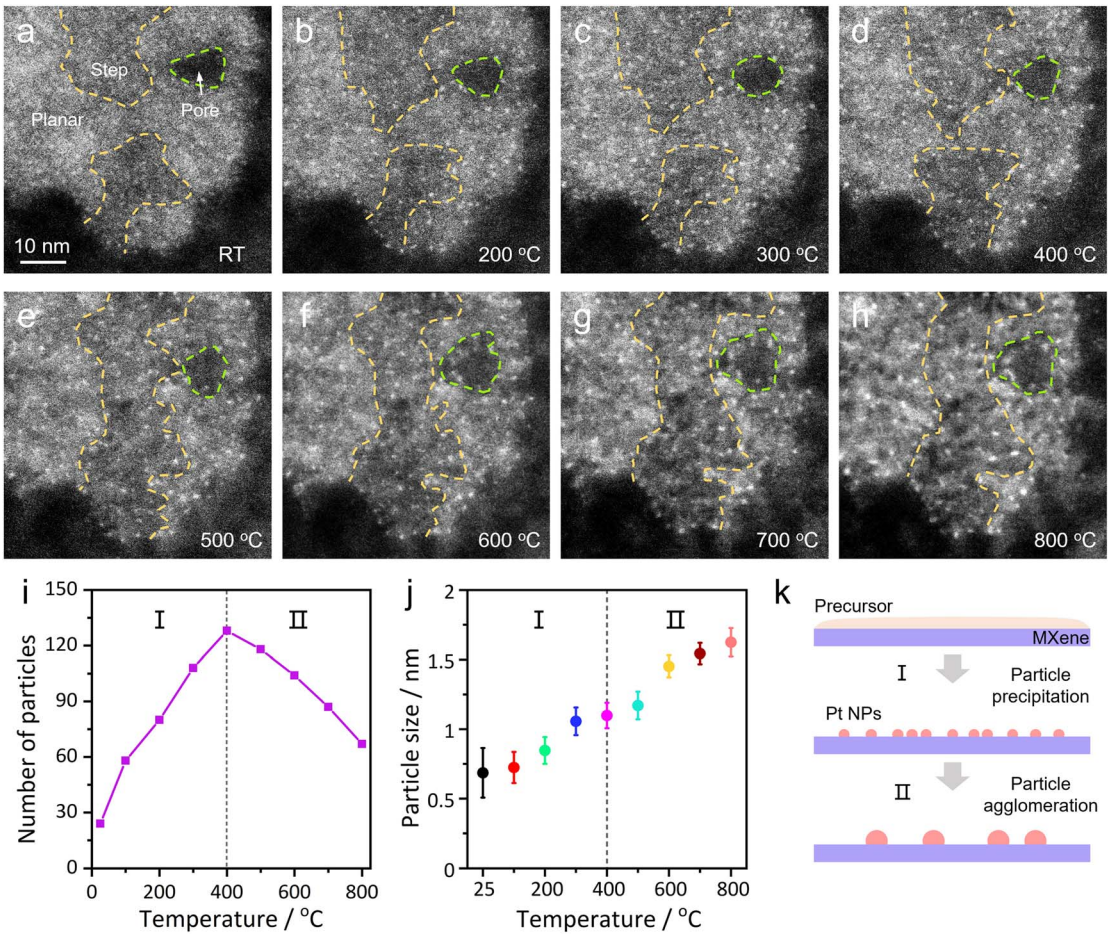


Fig. 2 Annealing behavior for Pt NPs on MXene. (a–h) *In situ* STEM image series showing the structural evolution of Pt NPs on a MXene flake against rising temperature. The pore edge and surface step in (a–h) are highlighted by green and yellow dotted lines, respectively. Scale bar in (a) also applies to (b–h). (i) Number of particles as a function of heating temperature for (a–h). (j) Average size of Pt NPs as a function of heating temperature across (a–h). (k) Schematic illustration on the thermal-induced dynamics for supported Pt NPs.

52.3% of the peak value (Stage II), which is a sintering process for NPs. Note that this maximum size is still within the empirical particle size range as high-performance nanocatalysts (<3 nm),[58] implying a limited sintering effect in this system. Two possible reasons are responsible for such a phenomenon: the crucial one is the uniform size distribution of Pt NPs, which has been considered as an effective strategy for achieving sinter resistance;[59] another noteworthy factor is the much stronger MSI at the Pt/MXene interface than those of other traditional supported catalysts (such as graphene-based systems, see discussion below).[60] One can also notice that the particle size tended to stabilize at 300–500 °C in Fig. 2j, which can be regarded as another sign for the transition of the above two stages. Moreover, the particle size distribution of Pt NPs at key temperature points has been documented to serve as an indicator to identify the sintering behavior, as shown in Fig. S5,† corresponding to the two stages above. Additionally, to investigate the effect of electron beam irradiation on our *in situ* experiment (which is always a serious issue in TEM observations),[38,61,62] a series of STEM images in Fig. S6† were captured, showing the evolution of Pt NPs on the MXene support without continuous beam irradiation; briefly, these NPs displayed similar sintering patterns with rising temperature to those of Fig. S5,† suggesting negligible beam effect in this heating experiment (and therefore the sintering dynamics is the intrinsic behavior for Pt/MXene upon controlled heating).

### Selection rule for the sintering mechanism of Pt NPs on MXene flakes

Particularly, we have further compared the number of Pt NPs on the planar surface and the steps/edges of MXene flakes during their sintering process and found an interesting surface topology-dependent sintering behavior. As shown in Fig. S7,† the density of NPs was almost the same on the planar surface and steps/edges of MXene at the beginning of sintering (400 °C), indicating an initially uniform particle distribution on MXene flakes. However, after heating at 800 °C, the Pt NPs on the planar surface of MXene underwent severe sintering (sintering ratio 53.5%). In contrast, the sintering ratio of Pt NPs on the steps/edges was only 35.7%, which is remarkably lower than that on the planar surface. The quantitative analysis on the change of particle number with heating temperature again

prompted faster sintering for Pt NPs on planar regions rather than those on steps/edges (Fig. S7c†), which directly inspired us to perform systematic investigation toward the mechanistic processes on these specific sites.

To understand the sintering mechanism of Pt NPs on the planar surface and steps/edges of the MXene support, we further observed the atomic-scale sintering behaviors of Pt NPs against annealing by *in situ* STEM. As shown in the sequential high-resolution STEM images in Fig. 3a, the directional migration for a pair of neighboring Pt NPs on the planar surface of a MXene flake was observed at 600 °C (as indicated by the pink circles), and eventually these two particles merged into a single one; the whole process took approximately 20 min. It is important to mention that we have repeatedly observed these coalescence events on the planar surface of MXene flakes, even upon heating to higher temperatures (see Fig. 3b and c for two more events at 700 and 800 °C, respectively). Undoubtedly, this kind of behavior is consistent with the concept of PMC as reported previously.[15] In stark contrast to the observations above, we have further noticed another kind of sintering behavior in which one NP grew up at the expense of another nearby NP while their positions remained almost unchanged (refer to Fig. 3d–f, as marked by blue circles at different temperatures); this phenomenon is, indeed, the typical OR mechanism. And of special attention, these Pt NPs that experienced the OR process were all supported on the steps/edges of the MXene surface.

Furthermore, we have recorded a sequence of STEM images in Fig. S8† to comparatively show these surface topology-dependent sintering mechanisms at the Pt/MXene interfaces. As indicated, two pairs of Pt NPs experienced overt PMC in the planar region whereas another two groups of Pt NPs underwent clear OR on the step edge of MXene during their sintering. Across our repeated observations, no exceptional case has been found; in alternative words, Pt NPs in the planar regions of MXene sinter *via* the PMC mechanism whereas those on the

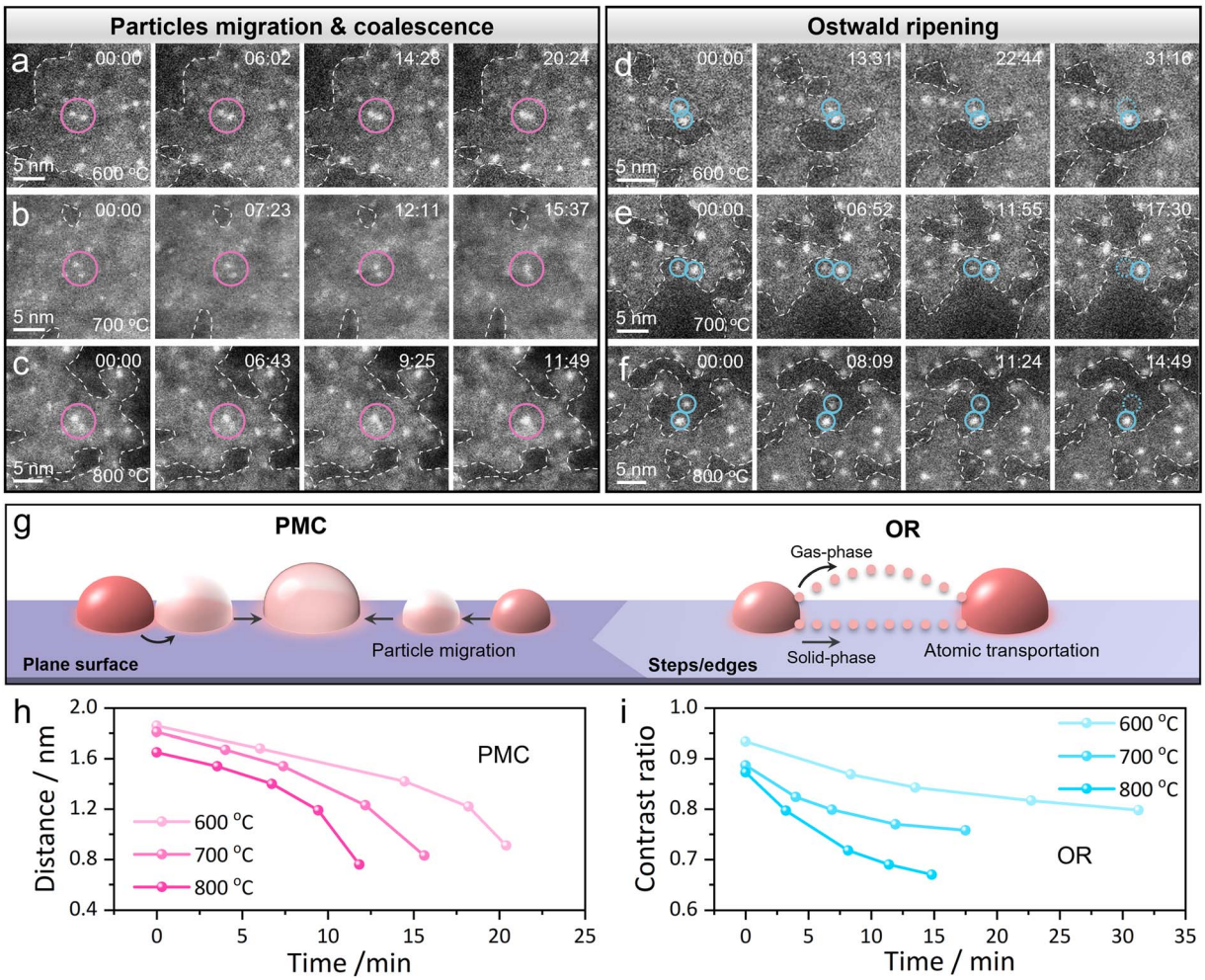


Fig. 3 Atomic-scale sintering dynamics for Pt NPs on MXene flakes. (a–c) Three independent STEM image series showing the PMC dynamics of Pt NPs on the planar surface of a MXene flake at (a) 600 °C (b) 700 °C and (c) 800 °C. (d–f) Three independent STEM image series showing the OR process of Pt NPs on the steps/edges of a MXene flake at (d) 600 °C, (e) 700 °C and (f) 800 °C. (g) Schematic of the PMC and OR mechanisms during sintering of Pt NPs affected by the surface topology of MXene flakes. (h) Plot showing the changing distance for the corresponding Pt NPs during PMC in (a–c) as a function of time. (i) Plot showing the changing contrast ratio for the corresponding Pt NPs during OR in (d–f) as a function of time.

steps/edges of MXene sinter *via* the OR pathway. On the planar surface of MXene flakes, the migration of Pt NPs dominates the sintering, which results in PMC processes as well as the rapid degradation of the nanocatalyst; yet the sintering of Pt NPs on the steps/edges of MXene flakes mainly concerns the diffusion of Pt atoms by either the solid-phase or gas-phase, leading to the occurrence of OR processes. Therefore, the two kinds of mechanisms jointly contributed to the size increase in Stage II of Fig. 2j. In this context, the selection rule for the sintering mechanism of Pt NPs on MXene flakes has been revealed (refer to Fig. 3g).

One may also notice that as the temperature increases (Fig. 3a–f), the time required for both PMC and OR processes of Pt NPs was substantially reduced, which is because that high temperature provides additional energy for particle migration and/or atom diffusion of Pt NPs. And we have also found that the PMC processes of Pt NPs are significantly faster than the OR processes at the same temperature, which can be simply explained by the distinct migrating media; one is NPs (in PMC) while the other is single atoms (in OR). To explore the thorough sintering kinetics of Pt NPs on MXene flakes, we quantitatively analyzed the corresponding sintering behaviors in the aforementioned two cases. For the PMC process, the sintering rate here is qualitatively described as the change of distances between two nearby Pt particles over time; the distance *vs.* time profiles for three pairs of Pt NPs on the planar MXene surface at different temperatures are shown in Fig. 3h (the sintering rate corresponds to the slope of the profile at every point). We found that the slope gradually increased over time, meaning that the rate of PMC is gradually accelerated during the sintering of two NPs. As the distance between two NPs decreases, the van der Waals attraction across them increases, bringing about the increasing sintering rate for PMC.[63] As for the OR process, the sintering rate here is qualitatively described as the contrast ratio of two NPs (as OR proceeds, one NP in a pair would get smaller while the other would get larger; accordingly, the contrast for the former would get darker and the later would get brighter in a STEM image), as shown in Fig. 3i (similarly, the sintering rate also corresponds to the slope of the contrast *vs.* time profile at every point). Upon this circumstance, the sintering rate of OR displays a gradually decelerated pattern, a result of the reduced atomic transportation rate as the atomic number of small NP decreases over time. Additionally, the sintering kinetics for both PMC and OR were obviously increased with the increase of annealing temperature; as the temperature increases, the kinetic energy of Pt atoms becomes higher, and thus the sintering between these NPs correspondingly becomes faster.

### Theoretical understanding on the selection of sintering mechanisms

As mentioned earlier in the Introduction, the site-dependent sintering mechanisms of Pt NPs should be attributed to the

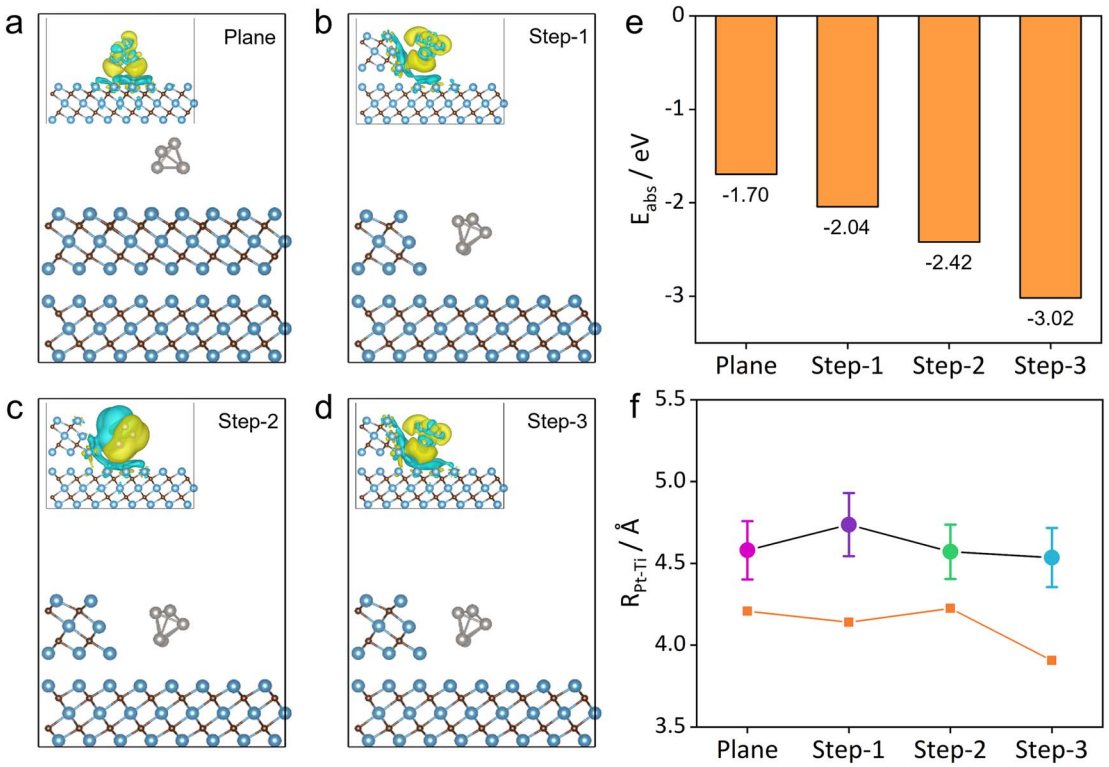


Fig. 4 Calculations on MSI between Pt NPs and different regions of MXene flakes. Models of Pt NPs adsorbed on (a) planar and (b–d) different positions of step regions; the insets present the corresponding side-view CCD (charge depletion: cyan, charge accumulation: yellow). (e) Binding energies of Pt NPs adsorbed on different positions of MXene flakes for (a–d). (f) Averaged distances between Pt and Ti atoms for Pt NPs adsorbed at the specific sites of MXene flakes for (a–d). The orange line in (f) show the corresponding shortest distance between Pt and Ti atoms in the models.

distinct MSIs for the planar and defective regions of MXene flakes according to the Sabatier principle.[26] Consequently, we try to understand the site-dependent MSI on the Pt/MXene interface by density functional theory (DFT) calculations to support the experimental findings.

As shown in Fig. 4a–d, the MSI between the Pt cluster (represented by a five-Pt atom-cluster, $Pt_5$) and MXene flakes leads to thermally stabilized $Pt_5$ clusters adsorbed at the planar or step (Step-1, Step-2 and Step-3) sites of the MXene surface, for which the DFT-derived adsorption energies are all negative (see Fig. 4e). The corresponding charge density differences (CDDs) in the insets of Fig. 4a–d (side views) and Fig. S9† (top views) show the accumulation of charge (yellow) in the interval of the $Pt_5$ cluster and MXene support, implying that the charge transfer on the steps of the $Pt_5$/MXene interface enhances MSI. It is notable that the $Pt_5$ cluster in the step regions undergoes charge transfer with more atomic sites of the MXene steps, whereas the $Pt_5$ cluster in the planar region only exhibits charge transfer with underlined Ti atoms on the surface of MXene. It is also evident that the CDD of $Pt_5$ adsorbed at the planar surface mainly involves three Pt atoms close to the plane, whereas those at the steps have four or even five atoms involved. In short, it is thus inferred that more significant charge transfer at the step sites leads to a stronger MSI between the Pt cluster and MXene support.

Moreover, the adsorption energies of the $Pt_5$ cluster at planar and step sites were evaluated by DFT calculation, which are −1.70, −2.04, −2.42 and −3.02 eV, respectively (Fig. 4e), which quantitatively demonstrate a stronger MSI for Pt clusters on the step sites of MXene than that on the planar surface. Besides, the averaged atomic distances (shorter than 5 Å) between Pt and Ti atoms ($R_{Pt–Ti}$) for these models and the corresponding shortest distances (orange line) are shown in Fig. 4f. Although the averaged $R_{Pt–Ti}$ shows no significant difference for these models, a slightly shorter averaged $R_{Pt–Ti}$ could be seen for Step-2 and Step-3. Moreover, the shortest $R_{Pt–Ti}$ of Step-3 is much smaller than that of the plane, inferring a stronger MSI between the Pt cluster and MXenes. In addition, the number of Pt–Ti bonds with $R_{Pt–Ti}$ shorter than 5.5 Å is more for the step models (more than 16) than that on the planar model (13) (Fig. S10†), further indicating that the steps of MXene have provided a stronger MSI with Pt even from a slightly long distance. In a thorough consideration of experimental observations and DFT results, the $Pt_5$ cluster on the planar site of MXene flakes possesses a relatively high adsorption energy yet a weak MSI, and thus the Pt NPs tend to become larger through the PMC mechanism. On the other hand, the relatively low adsorption energy for the $Pt_5$ cluster on the step sites of MXene induces a strong MSI for the OR pathway during sintering.

## Conclusions

Our systematic experimental and theoretical study on the sintering of Pt NPs supported by MXene flakes reveals that the sintering mechanism of Pt NPs depends on the surface topology of MXene flakes; the NPs on the steps/edges adopt the OR mechanism, whereas those on the planar surface prefer the PMC process (which usually causes rapid sintering in practical scenarios). The occurrence of these two types of sintering behaviour was confirmed to be induced by the different MSIs at the corresponding surface topologies of MXene flakes, which is consistent with the recently reported Sabatier principle. Moreover, our kinetic analysis demonstrated that the two sintering processes presented distinct tendencies of sintering rate over time. These results provide a guidance to tune MSI by introducing defects on supporting materials, which may pave the way for designing sintering-resistant metal nanocatalysts.

## Data availability

All data needed to evaluate the conclusions are present in the article and/or the ESI.†

## Author contributions

L. F. and C. H. conceived the idea and supervised the project. Y. Z. prepared TEM samples. J. H., J. C., and Z. Z. conducted TEM experiments and analyzed the data. C. Z. performed DFT calculations. L. F., C. H., J. H., and C. Z. wrote the manuscript with the help and input from all authors. All authors have given approval to the final version of the manuscript.

## Conflicts of interest

The authors declare no conflict of interest.

## Acknowledgements

This work was supported by the National Natural Science Foundation of China (22375081 and U21A20500) and the Natural Science Foundation of Jiangxi Province (20212ACB204016). L. F. also acknowledges the support from Nanchang University and the computational support from the High Performance Computing Center of Hebei University.

## References

1 Z. Liang, J. Shen, X. Xu, F. Li, J. Liu, B. Yuan, Y. Yu and M. Zhu, Advances in the development of single-atom catalysts for high-energy-density lithium-sulfur batteries, *Adv. Mater.*, 2022, **34**, 2200102.

2 F. Franco, C. Rettenmaier, H. S. Jeon and B. Roldan Cuenya, Transition metal-based catalysts for the electrochemical $CO_2$ reduction: From atoms and molecules to nanostructured materials, *Chem. Soc. Rev.*, 2020, **49**, 6884–6946.

3 X. Liu, J. Iocozzia, Y. Wang, X. Cui, Y. Chen, S. Zhao, Z. Li and Z. Lin, Noble metal–metal oxide nanohybrids with tailored nanostructures for efficient solar energy conversion, photocatalysis and environmental remediation, *Energy Environ. Sci.*, 2017, **10**, 402–434.

4 H. Yang, X. Wang, Q. Liu, A. Huang, X. Zhang, Y. Yu, Z. Zhuang, G. Li, Y. Li, Q. Peng, X. Chen, H. Xiao and C. Chen, Heterogeneous iridium single-atom molecular-

like catalysis for epoxidation of ethylene, *J. Am. Chem. Soc.*, 2023, **145**, 6658–6670.

5 Y. Nie, L. Li and Z. Wei, Recent advancements in Pt and Pt-free catalysts for oxygen reduction reaction, *Chem. Soc. Rev.*, 2015, **44**, 2168–2201.

6 Y. Li, H. Wang, X. Yang, T. O'Carroll and G. Wu, Designing and engineering atomically dispersed metal catalysts for $CO_2$ to CO conversion: from single to dual metal sites, *Angew. Chem., Int. Ed.*, 2024, **63**, e202317884.

7 A. K. Datye and M. Votsmeier, Opportunities and challenges in the development of advanced materials for emission control catalysts, *Nat. Mater.*, 2021, **20**, 1049–1059.

8 Y. Liu, Z. Liu, Y. Hui, L. Wang, J. Zhang, X. Yi, W. Chen, C. Wang, H. Wang, Y. Qin, L. Song, A. Zheng and F.-S. Xiao, Rhodium nanoparticles supported on silanol-rich zeolites beyond the homogeneous Wilkinson's catalyst for hydroformylation of olefins, *Nat. Commun.*, 2023, **14**, 2531.

9 X. Ge, D. Xie, R.-f. Cheng, W. Chen, C. Chen, F. Zhou, X. Wang, J.-j. Chen, G.-p. Sheng and Y. Wu, Three-dimensional welded $Mn_1$ site catalysts with nearly 100% singlet oxygen fabrication for contaminant elimination, *Precis. Chem.*, 2023, **1**, 153–160.

10 S. Arcidiacono, N. R. Bieri, D. Poulikakos and C. P. Grigoropoulos, On the coalescence of gold nanoparticles, *Int. J. Multiphase Flow*, 2004, **30**, 979–994.

11 C. T. Campbell, The energetics of supported metal nanoparticles: Relationships to sintering rates and catalytic activity, *Acc. Chem. Res.*, 2013, **46**, 1712–1719.

12 A. T. DeLaRiva, T. W. Hansen, S. R. Challa and A. K. Datye, In situ transmission electron microscopy of catalyst sintering, *J. Catal.*, 2013, **308**, 291–305.

13 C. T. Campbell, S. C. Parker and D. E. Starr, The effect of size-dependent nanoparticle energetics on catalyst sintering, *Science*, 2002, **298**, 811–814.

14 M. Rahmati, M. S. Safdari, T. H. Fletcher, M. D. Argyle and C. H. Bartholomew, Chemical and thermal sintering of supported metals with emphasis on cobalt catalysts during fischer-tropsch synthesis, *Chem. Rev.*, 2020, **120**, 4455–4533.

15 T. W. Hansen, A. T. Delariva, S. R. Challa and A. K. Datye, Sintering of catalytic nanoparticles: Particle migration or Ostwald ripening?, *Acc. Chem. Res.*, 2013, **46**, 1720–1730.

16 R. Ouyang, J. X. Liu and W. X. Li, Atomistic theory of Ostwald ripening and disintegration of supported metal particles under reaction conditions, *J. Am. Chem. Soc.*, 2013, **135**, 1760–1771.

17 S. R. Challa, A. T. Delariva, T. W. Hansen, S. Helveg, J. Sehested, P. L. Hansen, F. Garzon and A. K. Datye, Relating rates of catalyst sintering to the disappearance of individual nanoparticles during Ostwald ripening, *J. Am. Chem. Soc.*, 2011, **133**, 20672–20675.

18 S. B. Simonsen, I. Chorkendorff, S. Dahl, M. Skoglundh, J. Sehested and S. Helveg, Direct observations of oxygen-induced platinum nanoparticle ripening studied by in situ TEM, *J. Am. Chem. Soc.*, 2010, **132**, 7968–7975.

19 M. A. Asoro, D. Kovar, Y. Shao-Horn, L. F. Allard and P. J. Ferreira, Coalescence and sintering of Pt nanoparticles: In situ observation by aberration-corrected HAADF STEM, *Nanotechnology*, 2010, **21**, 025701.

20 W. Yuan, D. Zhang, Y. Ou, K. Fang, B. Zhu, H. Yang, T. W. Hansen, J. B. Wagner, Z. Zhang, Y. Gao and Y. Wang, Direct in situ TEM visualization and insight into the facet-dependent sintering behaviors of gold on $TiO_2$, *Angew. Chem., Int. Ed.*, 2018, **57**, 16827–16831.

21 L. Lin, J. Liu, X. Liu, Z. Gao, N. Rui, S. Yao, F. Zhang, M. Wang, C. Liu, L. Han, F. Yang, S. Zhang, X. D. Wen, S. D. Senanayake, Y. Wu, X. Li, J. A. Rodriguez and D. Ma, Reversing sintering effect of Ni particles on $\gamma$-$Mo_2N$ via strong metal support interaction, *Nat. Commun.*, 2021, **12**, 6978.

22 T. W. van Deelen, C. Hernández Mejía and K. P. de Jong, Control of metal-support interactions in heterogeneous catalysts to enhance activity and selectivity, *Nat. Catal.*, 2019, **2**, 955–970.

23 S. Li, Y. Xia, Y. Ou, Z. Wu, Z. Jin, L. Wang, X. Meng, Z.-K. Han, W. Yuan, Y. Jiang, D. J. Wales, H. Yang and Y. Wang, Unusual facet-dependent sintering in Pd–$TiO_2$ catalysts revealed by theory and experiment, *ACS Catal.*, 2024, **14**, 1608–1619.

24 S. Lin, Z. Hao, J. Shen, X. Chang, S. Huang, M. Li and X. Ma, Enhancing the $CO_2$ methanation activity of Ni/$CeO_2$ via activation treatment-determined metal-support interaction, *J. Energy Chem.*, 2021, **59**, 334–342.

25 H. Xin, L. Lin, R. Li, D. Li, T. Song, R. Mu, Q. Fu and X. Bao, Overturning $CO_2$ hydrogenation selectivity with high activity via reaction-induced strong metal-support interactions, *J. Am. Chem. Soc.*, 2022, **144**, 4874–4882.

26 S. Hu and W.-X. Li, Sabatier principle of metal-support interaction for design of ultrastable metal nanocatalysts, *Science*, 2021, **374**, 1360–1365.

27 J.-C. Liu, L. Luo, H. Xiao, J. Zhu, Y. He and J. Li, Metal affinity of support dictates sintering of gold catalysts, *J. Am. Chem. Soc.*, 2022, **144**, 20601–20609.

28 Z. Luo, G. Zhao, H. Pan and W. Sun, Strong metal-support interaction in heterogeneous catalysts, *Adv. Energy Mater.*, 2022, **12**, 2201395.

29 P. Liu, A. Klyushin, P. Chandramathy Surendran, A. Fedorov, W. Xie, C. Zeng and X. Huang, Carbon encapsulation of supported metallic iridium nanoparticles: an in situ transmission electron microscopy study and implications for hydrogen evolution reaction, *ACS Nano*, 2023, **17**, 24395–24403.

30 J. Wang, C. Hu, L. Wang, Y. Yuan, K. Zhu, Q. Zhang, L. Yang, J. Lu and Z. Bai, Suppressing thermal migration by fine-tuned metal-support interaction of iron single-atom catalyst for efficient ORR, *Adv. Funct. Mater.*, 2023, **33**, 2304277.

31 A. Beck, H. Frey, X. Huang, A. H. Clark, E. D. Goodman, M. Cargnello, M. Willinger and J. A. van Bokhoven, Controlling the strong metal-support interaction overlayer structure in Pt/$TiO_2$ catalysts prevents particle evaporation, *Angew. Chem., Int. Ed.*, 2023, **62**, e202301468.

32 W. Peng, Y.-R. Lu, H. Lin, M. Peng, T.-S. Chan, A. Pan and Y. Tan, Sulfur-stabilizing ultrafine high-entropy alloy

nanoparticles on MXene for highly efficient ethanol electrooxidation, *ACS Nano*, 2023, **17**, 22691–22700.

33 P. Yuan, X. Liao, H. Cui, F. Hao, W. Xiong, H. a. Luo, Y. Lv and P. Liu, Decarboxylation-induced defects in MOF-derived Ni@C catalysts for efficient chemoselective hydrogenation of nitrocyclohexane to cyclohexanone oxime, *ACS Catal.*, 2023, **13**, 3224–3241.

34 Z. Lang, Z. Zhuang, S. Li, L. Xia, Y. Zhao, Y. Zhao, C. Han and L. Zhou, MXene surface terminations enable strong metal-support interactions for efficient methanol oxidation on palladium, *ACS Appl. Mater. Interfaces*, 2020, **12**, 2400–2406.

35 S. Hwang, X. Chen, G. Zhou and D. Su, In situ transmission electron microscopy on energy-related catalysis, *Adv. Energy Mater.*, 2019, **10**, 1902105.

36 H. Zhao, Y. Zhu, H. Ye, Y. He, H. Li, Y. Sun, F. Yang and R. Wang, Atomic-scale structure dynamics of nanocrystals revealed by in situ and environmental transmission electron microscopy, *Adv. Mater.*, 2022, **35**, 2206911.

37 L. Fei, S. Lei, W. B. Zhang, W. Lu, Z. Lin, C. H. Lam, Y. Chai and Y. Wang, Direct TEM observations of growth mechanisms of two-dimensional $MoS_2$ flakes, *Nat. Commun.*, 2016, **7**, 12206.

38 Z. Zhang, Y. Tang, Y. Ying, J. Guo, M. Gan, Y. Jiang, C. Xing, S. Pan, M. Xu, Y. Zhou, H. Zhang, C. W. Leung, H. Huang, C. L. Mak and L. Fei, Multistep nucleation visualized during solid-state crystallization, *Mater. Horiz.*, 2022, **9**, 1670–1678.

39 J. Huang, Z. Zhang, Y. Ying, M. Gan, H. Huang and L. Fei, Atomic-scale mechanisms on the stepwise growth of $Mo_xW_{1-x}S_2$ into hexagonal flakes, *Chem. Commun.*, 2022, **58**, 9746–9749.

40 B. R. Anne, J. Kundu, M. K. Kabiraz, J. Kim, D. Cho and S. I. Choi, A review on MXene as promising support materials for oxygen evolution reaction catalysts, *Adv. Funct. Mater.*, 2023, **33**, 2306100.

41 X. Wang, J. Ding, W. Song, X. Yang, T. Zhang, Z. Huang, H. Wang, X. Han and W. Hu, Cation vacancy clusters in $Ti_3C_2T_x$ MXene induce ultra-strong interaction with noble metal clusters for efficient electrocatalytic hydrogen evolution, *Adv. Energy Mater.*, 2023, **13**, 2300148.

42 Y. Zhao, J. Zhang, X. Guo, X. Cao, S. Wang, H. Liu and G. Wang, Engineering strategies and active site identification of MXene-based catalysts for electrochemical conversion reactions, *Chem. Soc. Rev.*, 2023, **52**, 3215–3264.

43 W. Kong, J. Deng and L. Li, Recent advances in noble metal MXene-based catalysts for electrocatalysis, *J. Mater. Chem. A*, 2022, **10**, 14674–14691.

44 Q. Zhong, Y. Li and G. Zhang, Two-dimensional MXene-based and MXene-derived photocatalysts: Recent developments and perspectives, *Chem. Eng. J.*, 2021, **409**, 128099.

45 D. Zhao, Z. Chen, W. Yang, S. Liu, X. Zhang, Y. Yu, W. C. Cheong, L. Zheng, F. Ren, G. Ying, X. Cao, D. Wang, Q. Peng, G. Wang and C. Chen, MXene ($Ti_3C_2$) vacancy-confined single-atom catalyst for efficient functionalization of $CO_2$, *J. Am. Chem. Soc.*, 2019, **141**, 4086–4093.

46 X. Sang, Y. Xie, M. W. Lin, M. Alhabeb, K. L. Van Aken, Y. Gogotsi, P. R. C. Kent, K. Xiao and R. R. Unocic, Atomic defects in monolayer titanium carbide ($Ti_3C_2T_x$) MXene, *ACS Nano*, 2016, **10**, 9193–9200.

47 X. Sang, D. Yilmaz, Y. Xie, M. Alhabeb, B. Anasori, X. Li, K. Xiao, P. R. C. Kent, A. van Duin, Y. Gogotsi and R. R. Unocic, Atomic defects and edge structure in single-layer $Ti_3C_2T_x$ MXene, *Microsc. Microanal.*, 2017, **23**, 1704–1705.

48 M. Malaki, A. Maleki and R. S. Varma, MXenes and ultrasonication, *J. Mater. Chem. A*, 2019, **7**, 10843–10857.

49 Z. Zhang, Y. Ying, M. Xu, C. Zhang, Z. Rao, S. Ke, Y. Zhou, H. Huang and L. Fei, Atomic steps induce the aligned growth of ice crystals on graphite surfaces, *Nano Lett.*, 2020, **20**, 8112–8119.

50 M. Vaarkamp, J. V. Grondelle, J. T. Miller, D. J. Sajkowski, F. S. Modica, G. S. Lane, B. C. Gates and D. C. Koningsberger, Pt clusters in BaKL zeolite: Characterization by transmission electron microscopy, hydrogen chemisorption, and X-ray absorption spectroscopy, *Catal. Lett.*, 1990, **6**, 369–382.

51 H. Wang, Y. Wu, X. Yuan, G. Zeng, J. Zhou, X. Wang and J. W. Chew, Clay-inspired MXene-based electrochemical devices and photo-electrocatalyst: State-of-the-art progresses and challenges, *Adv. Mater.*, 2018, **30**, 1704561.

52 C. E. Shuck, A. Sarycheva, M. Anayee, A. Levitt, Y. Zhu, S. Uzun, V. Balitskiy, V. Zahorodna, O. Gogotsi and Y. Gogotsi, Scalable synthesis of $Ti_3C_2T_x$ MXene, *Adv. Eng. Mater.*, 2020, **22**, 1901241.

53 H. Ye, F. Yang, Y. Sun and R. Wang, Atom-resolved investigation on dynamic nucleation and growth of platinum nanocrystals, *Small Methods*, 2022, **6**, e2200171.

54 H. Li, L. Wang, Y. Dai, Z. Pu, Z. Lao, Y. Chen, M. Wang, X. Zheng, J. Zhu, W. Zhang, R. Si, C. Ma and J. Zeng, Synergetic interaction between neighbouring platinum monomers in $CO_2$ hydrogenation, *Nat. Nanotechnol.*, 2018, **13**, 411–417.

55 J. N. Tiwari, S. Sultan, C. W. Myung, T. Yoon, N. Li, M. Ha, A. M. Harzandi, H. J. Park, D. Y. Kim, S. S. Chandrasekaran, W. G. Lee, V. Vij, H. Kang, T. J. Shin, H. S. Shin, G. Lee, Z. Lee and K. S. Kim, Multicomponent electrocatalyst with ultralow Pt loading and high hydrogen evolution activity, *Nat. Energy*, 2018, **3**, 773–782.

56 X. Sang, Y. Xie, D. E. Yilmaz, R. Lotfi, M. Alhabeb, A. Ostadhossein, B. Anasori, W. Sun, X. Li, K. Xiao, P. R. C. Kent, A. C. T. van Duin, Y. Gogotsi and R. R. Unocic, In situ atomistic insight into the growth mechanisms of single layer 2D transition metal carbides, *Nat. Commun.*, 2018, **9**, 2266.

57 V. P. Nguyen, M. Lim, K.-S. Kim, J.-H. Kim, J. S. Park, J. M. Yuk and S.-M. Lee, Drastically increased electrical and thermal conductivities of Pt-infiltrated MXenes, *J. Mater. Chem. A*, 2021, **9**, 10739–10746.

58 L. Liu and A. Corma, Metal catalysts for heterogeneous catalysis: From single atoms to nanoclusters and nanoparticles, *Chem. Rev.*, 2018, **118**, 4981–5079.

59 Y. Dai, P. Lu, Z. Cao, C. T. Campbell and Y. Xia, The physical chemistry and materials science behind sinter-resistant catalysts, *Chem. Soc. Rev.*, 2018, **47**, 4314–4331.
60 S. G. Peera, C. Liu, A. K. Sahu, M. Selvaraj, M. C. Rao, T. G. Lee, R. Koutavarapu, J. Shim and L. Singh, Recent advances on MXene-based electrocatalysts toward oxygen reduction reaction: A focused review, *Adv. Mater. Interfaces*, 2021, **8**, 2100975.
61 Z. Zhang, J. Qiang, S. Wang, M. Xu, M. Gan, Z. Rao, T. Tian, S. Ke, Y. Zhou, Y. Hu, C. W. Leung, C. L. Mak and L. Fei, Visualization of bubble nucleation and growth confined in 2D flakes, *Small*, 2021, **17**, 2103301.
62 X. Zhang, K. Hattar, Y. Chen, L. Shao, J. Li, C. Sun, K. Yu, N. Li, M. L. Taheri, H. Wang, J. Wang and M. Nastasi, Radiation damage in nanostructured materials, *Prog. Mater. Sci.*, 2018, **96**, 217–321.
63 S. Shrestha, B. Wang and P. Dutta, Nanoparticle processing: Understanding and controlling aggregation, *Adv. Colloid Interface Sci.*, 2020, **279**, 102162.